3

Occurrence of tuite and ahrensite in Zagami and their significance

for shock-histories recorded in martian meteorites

5

6   Lixin Gu[1, 2, 3], Sen Hu[1, 3*], Mahesh Anand[4, 5], Xu Tang[1, 2, 3], Jianglong Ji[1, 3, 6], Bin Zhang [7],

7   Nian Wang[1, 3, 6], Yangting Lin[1, 3, 6]

8

9   [1]Key Laboratory of Earth and Planetary Physics, Institute of Geology and Geophysics,

10   Chinese Academy of Sciences, Beijing, 100029, China

11   [2]Electron Microscopy Laboratory, Institute of Geology and Geophysics, Chinese Academy of

12   Sciences, Beijing, 100029, China

13   [3]Innovation Academy for Earth Science, Chinese Academy of Sciences, Beijing 10029, China

14   [4]School of Physics Sciences, The Open University, Milton Keynes, MK5 6AA, UK

15   [5]Department of Earth Sciences, The Natural History Museum, London, SW7 5BD, UK

16   [6]University of Chinese Academy of Sciences, Beijing, 100049, China

17   [7]Analytical and Testing Center of Chongqing University, Chongqing 400044, China

18

19   *Corresponding author. E-mail: husen@mail.iggcas.ac.cn. 19 Beituchengxi Road

20   Chaoyang District, Beijing, China, 100029.

21

22

23

24 ABSTRACT

25   We report on the discovery of two high-pressure minerals, tuite and ahrensite,

26 located in two small shock-induced melt pockets (SIMP #1 and #2) in the Zagami

27 martian meteorite, coexisting with granular and acicular stishovite and seifertite. Tuite

28 identified in this study has two formation pathways: decomposition of apatite and

29 transformation of merrillite under high P-T conditions. Chlorine bearing products,

30 presumably derived from the decomposition of apatite, are concentrated along the

31 grain boundaries of tuite grains. Nanocrystalline that ahrensite occurred within the

32 pyroxene clast in SIMP #2 is likely to be a decomposition product of pigeonite under

33 high P-T conditions by a solid state transformation mechanism. The pressure and

34 temperature conditions estimated from the high-pressure minerals in the shock

35 induced melt pockets are $\sim$ 12-22 GPa and $\sim$ 1100-1500 °C, respectively, although

36 previous estimates of peak shock pressure are higher. This discrepancy probably

37 represents the shift of kinetic relative to thermodynamic phase boundaries in the

38 particular, comparatively small hotspot that we examine here rather than a principal

39 disagreement about the peak shock conditions.

40 **Keywords**: tuite; ahrensite; Zagami; martian meteorite; high-pressure minerals

41

1. INTRODUCTION

Many meteorites from Mars (Baziotis et al., 2013; Hu et al., 2020; Miyahara et al., 2016; Sharp et al., 2019), the Moon (Kayama et al., 2018; Miyahara et al., 2013; Ohtani et al., 2011; Zhang et al., 2010), Howardite-eucrite-diogenite (HED) meteorites (Miyahara et al., 2014; Pang et al., 2018; Pang et al., 2016), and ordinary chondrites (e.g., Binns et al., 1969; Chen et al., 1996; Sharp and DeCarli, 2006; Stöffler et al., 1991; Tschauner et al., 2014) are highly shocked, as evidenced by the observation of deformation in constituent minerals and formation of various high-pressure phases. The high-pressure minerals discovered in these extraterrestrial natural samples could reveal the impact history on their parent bodies and provide insights into the phase transformation mechanisms in the interior of Earth (Petrova and Grokhovsky, 2019). To date, high-pressure polymorphs of olivine (Binns et al., 1969; Chen et al., 2004; Ma et al., 2016; Miyahara et al., 2008; Putnis and Price, 1979), pyroxene (Chen et al., 1996; Sharp et al., 1997; Tomioka and Fujino, 1999; Tschauner et al., 2014), feldspar (Fritz et al., 2020; Gillet et al., 2000; Liu, 1978; Ma et al., 2018; Tschauner et al., 2021), zircon (Glass et al., 2002; Xing et al., 2020), silica (El Goresy et al., 2004; El Goresy et al., 2000b; Hu et al., 2020; Miyahara et al., 2014; Ohtani et al., 2011; Sharp et al., 1999), chromite (Chen et al., 2003; Ma et al., 2019), and Ca phosphate (Wang et al., 2017; Xie et al., 2002; Xie et al., 2013) have been reported from various meteorites displaying shock effects.

Tuite, a high-pressure polymorph of Ca-phosphate with the structure of γ-$Ca_3(PO_4)_2$, is of great significance as a host for larger lithophile elements in the deep Earth (Skelton and Walker, 2017; Xie et al., 2002). It has been reported in shocked chondrites (Hu and Sharp, 2016; Xie et al., 2016; Xie et al., 2002), martian meteorites (Baziotis et al., 2013; Boonsue and Spray, 2012; Fritz and Greshake, 2009; Wang et al., 2017), and iron meteorites (Litasov and Podgornykh, 2017). Tuite was proposed to form from decomposition of apatite or solid-state phase transformation of merrillite (Murayama et al., 1986; Xie et al., 2016; Xie et al., 2002; Xie et al., 2013). Some tuite grains in Suizhou (Xie et al., 2016) and NWA 7755 (Wang et al., 2017) were found coexisting with Cl-rich apatite, with a Cl content of up to ~ 3.9 wt%, consistent with possibility that they formed through decomposition of adjacent chlorapatite. However, the ideal formula of tuite, $Ca_3(PO_4)_2$, similar to extraterrestrial merrillite, does not contain Cl or other halogens (Jolliff et al., 2006; McCubbin et al., 2014). A reasonable

75   explanation is that the Cl measured in tuite is derived from partial decomposition of

76   precursor apatite (Wang et al., 2017; Xie et al., 2016). Another explanation is that

77   there are some other Cl-bearing products, *e.g.*, $CaCl_2$, accompanying the formation of

78   tuite by decomposition of apatite (Murayama et al., 1986; Xie et al., 2013). However,

79   the details about how these Cl-bearing products exist are still unclear, which

80   are crucial for better understanding the transformation mechanism of apatite during

81   shock metamorphism (Xie et al., 2013).

82   Ahrensite, a natural γ-Fe_2SiO_4, has been previously reported from shock-melt

83   pockets in ordinary chondrites (Feng et al., 2011; Xie et al., 2002b), lunar basalts

84   (Zhang et al., 2010), and olivine-phyric shergottites (Ma et al., 2016; Sharp et al.,

85   2019). It was thought to be formed either via fractional crystallization from shock-

86   induced melt (Miyahara et al., 2009; Xie et al., 2002b) or by solid-state transformation

87   of olivine (Chen et al., 2004). Theoretically, ahrensite and/or ringwoodite can also be

88   formed from decomposition of pyroxene at pressure of 18–22 GPa and temperature of

89   ~ 1300 °C (Gasparik, 1990; Tomioka and Miyahara, 2017), but this pyroxene-derived

90   formation mechanism was not reported until this study.

91   The Zagami martian meteorite is a basaltic shergottite, mainly consisting of

92   pyroxene (mostly augite and pigeonite) and maskelynite with minor amounts of

93   ilmenite, pyrrhotite, phosphate, and titanomagnetite (Langenhorst et al., 1991; McCoy

94   et al., 1992). Several high-pressure phases have been observed in Zagami, including

95   stishovite (Langenhorst and Poirier, 2000b), seifertite (El Goresy et al., 2008),

96   liebermannite (Ma et al., 2018), zagamiite-donwilhelmsite (Beck et al., 2004; Fritz et

97   al., 2020; Tschauner and Ma, 2017), and akimotoite (Langenhorst and Poirier, 2000b).

98   These high-pressure polymorphs substantiate that Zagami was highly-shocked on

99   Mars. The peak shock pressure of Zagami was estimated to be ~ 30 GPa using shock

100   barometers (Langenhorst et al., 1991; Stöffler et al., 1986). Based on the high-

101   pressure mineral assemblages and their phase diagrams, the shock pressure and

102   temperature have been reported to ~20-25 GPa and ~ 1900-2200 °C, respectively, for

103   shock-induced hotspots and melt veins (Beck et al., 2004; El Goresy et al., 2000a; El

104   Goresy et al., 2008; El Goresy et al., 2013; Langenhorst and Poirier, 2000a;

105   Langenhorst and Poirier, 2000b; Ma, 2018; Ma et al., 2016; Ma et al., 2015; Ma et al.,

106   2018).

107   In this study, we report new occurrences of tuite and ahrensite associated with

108   stishovite and seifertite in Zagami. A combined investigation using scanning electron

109   microscope, electron microprobe, transmission electron microscope, and Raman

110   spectroscopy were conducted to reveal the textural, physical, and chemical

111   characteristics of these high-pressure minerals for shedding light on their formation

112   mechanism and conditions during a hypervelocity impact event experienced on the

113   parent body.

114   2. Materials and experimental Methods

115   2.1. Sample and SEM

116   Petrographic observations of Zagami (P24058) were carried out by

117   backscattered electron (BSE) imaging using the Thermofisher Apreo field

118   emission scanning electron microscope (FE-SEM) with a Bruker XFlash 60

119   energy dispersive spectrometer (EDS) detector at the Institute of Geology and

120   Geophysics, Chinese Academy of Sciences (IGGCAS), Beijing, China. The

121   instrument was operated at accelerating voltages of 10~15 kV with beam

122   currents of 1.6-13 nA. Minerals distribution map was conducted using Maps and

123   Nanomin software.

124   2.2. EPMA

125   Quantitative chemical compositions of phosphates and silicates were measured

126   using JEOL 8100 electron probe microanalyzer (EPMA) with four Wavelength

127   Dispersive Spectrometers (WDS) at IGGCAS. The instrument was operated at an

128   accelerating voltage of 15 kV, a probe current of 20 nA, and a ~1-2 μm spot size. The

129   standards used were natural and synthetic minerals: albite for Na Si and Al, diopside

130   for Mg and Ca, fluorite for F, apatite for P, tugtupite for Cl, hematite for Fe, bustamite

131   for Mn, sanidine for K, rutile for Ti and Cr_2O_3 for Cr. All data were processed with

132   the ZAF correction procedure supplied with the JEOL microprobe. Detection limits

133   are: 0.01 wt% for Mg and Cl, 0.02 wt% for Si, Na, F, Si, Cr, Al, Mg, Fe, Ca, Ni and

134   Ti, 0.04 wt% for P.

135   2.3. Raman

136   The Raman spectra of minerals were collected using a WITec alpha 300R

137   confocal Raman system. An optical microscope with objective of 0.9 NA and 100×

138   magnification was used to focus the excitation laser beam of 532 nm excitation

139   wavelength on the target phases. Initially, to avoid damage of high-pressure minerals,

    a 2 mW laser power was used to identify the high pressure minerals. Ultimately,

140 Raman spectra were acquired with a total integration time of 90 s with a 5 mW laser

141 power. A 20 mW laser power was used for removing the thick coating of carbon

142 that was applied in order to obtain a high spatial resolution BSE image on the

143 tuite aggregate.

144 **2.4. FIB and TEM**

145 Two transmission electron microscopy (TEM) foils containing high-pressure

146 minerals were prepared using Zeiss Auriga Compact focused ion beam (FIB) dual

147 beam system equipped with an Omniprobe 200 micromanipulator. Ion milling was

148 carried out with an accelerating voltage of 5-30 kV and various beam currents (50 pA

149 to 2 nA). The final foils were about ~ 100 nm in thickness. It took about 2.5 hours to

150 prepare a foil. The microtextural and mineralogical characterizations of these two

151 foils were performed using JEM 2100 TEM at IGGCAS and FEI Talos 200S at

152 Chongqing University. All the TEM observations were performed at 200 kV.

153 Conventional bright field (BF) TEM and high angle annular dark field (HAADF)

154 imaging were performed to record the petrographic textures of the TEM foils.

155 Selected area electron diffraction (SAED) and high-resolution TEM (HRTEM)

156 images were used to determine the mineral structures; meanwhile, energy

157 dispersive X-ray spectroscopy (EDS) was used to determine chemical compositions

158 of minerals. The detection limits is about ~0.1 wt%.

159 **3. RESULTS**

160 **3.1. Petrography of Zagami meteorite**

161 Zagami studied in this work has a typical porphyritic texture with a partial fusion

162 crust (Fig. 1), mainly composed of pyroxene (71.6 area%) and maskelynite (24.1

163 area%) with minor phosphate (1.6 area%), silica (1.2 area%), and opaque minerals

164 (pyrrhotite, ilmenite and titanomagnetite, 1.4 area%). Pyroxene displays patchy

165 zoning with pigeonite cores, augite rims, and often an overgrowth of Fe-rich

166 layer. Most pyroxene grains display exsolution lamella. Merrillite and Cl-rich apatite

167 are the major phosphates and they are usually found in the interstitial regions with

168 grain sizes up to 200-300 μm in width (Fig. 1). The chemical compositions of

169 pyroxene and maskelynite are $Fs_{32-53}Wo_{11-33}En_{34-38}$ and $An_{36-52}Ab_{46-60}Or_{2-3}$,

170 respectively (Table 1). Merrillite usually contains minor amount of Na_2O (1.2-1.5 wt

171 %), MgO (2.2-3.1 wt%), and FeO (2.6-3.6 wt%) without any detectable F and Cl

(Table 1). Apatite grains from

7

172   Zagami have Cl and F contents ranging from 0.2 to 4.1 wt% and from 0.1 to 1.8 wt%

173   (Table 1), respectively.

174   Two small shock-induced melt pockets (< 200 μm^2) were observed across the

175   section, as indicated by two square regions (Fig. 1, 2 and 6). Four high-pressure

176   polymorphs of silica, phosphate, and olivine are identified in the two shock-induced

177   melt pockets (Sections 3.2 and 3.3). In addition, all of the silica grains occurring with

178   maskelynite throughout the host rock have been transformed into high-pressure

179   polymorphs of silica: stishovite and seifertite.

3.2. High-pressure polymorphs in shock induced melt pocket #1

181   The shock-induced melt pocket #1 (SIMP#1) is located at the interface region

182   between a maskelynite and a pyroxene (Fig. 2a). SIMP#1 is mainly composed of a

183   fine-grained matrix which also contains some small silica grains (darkest phases in the

184   BSE image) and a phosphate clast (Fig. 2a). The higher magnification BSE images

185   show abundant euhedral silica grains with grain sizes less than 2 μm, embedded in the

186   glassy matrix (Figs. 2b and 2d-f). These silica grains in SIMP#1 are stishovite. The

187   phosphate clast in SIMP#1 is an aggregate of submicrometer-sized tuite showing a

188   major Raman band at 975 cm^{-1} with minor weak bands at 412, 577, 1001, and 1094

189   cm^{-1} (Figs. 2d and 3c). In addition, there are many bright nanometer sized particles

190   located at the triple junction of tuite grains (Fig. 2e-f). The adjacent coarse silica grain

191   showing lamellar textures has transformed into seifertite and stishovite with Raman

192   bands at 231, 513, and 750 cm^{-1} (Figs. 2a and 3b). In contrast, the apatite inclusion

193   with characteristics of Raman bands at 959 cm^{-1} (Fig. 3d) in the coarse silica grain has

194   not transformed into tuite (Fig. 2a). However, an elongate apatite grain close to SIMP

195   #1 has partially transformed into tuite (Figs. 2a and 3c). The host pyroxene grain

196   displays exsolution lamellae without any signs of high-pressure polymorphs (Fig. 3e)

197   and the plagioclase has been transformed into maskelynite.

198   A focused ion beam (FIB) foil (FIB #1) was extracted on the tuite aggregate for a

199   detailed petrographic investigation of SIMP #1 (Fig. 2d). FIB #1 is ~ 5 μm in width

200   and ~ 13 μm in length (Fig. 4a). The secondary electron image after extraction

201   displays abundant euhedral silica grains in the SIMP #1 (Fig. 4a). The tuite grains are

202   less than 500 nm in length with subhedral shapes assembled together as an aggregate

203   (Fig. 4b). Many bright spots less than 50 nm are located along the grain boundaries of

204   tuite grains, mainly at the triple junctions (Fig. 4b). The groundmass of FIB #1 is

205   dominantly composed of silicate glasses containing some euhedral stishovite grains

206   less than ~ 200 nm, as identified by the TEM SAED patterns (Fig. 4b-d). Most

207   stishovite grains identified in this location were easily vitrified under the TEM beams.

208   The HAADF-EDS mapping images of tuite aggregate outlined by the white

209   rectangle in Fig. 4b indicate that tuite grains are homogeneous in O, P, and Ca with

210   some hotspots of Cl (Fig. 5). The bright spots along the boundaries (dashed white

211   lines in Fig. 5a-e) of tuite grains are significantly Fe-enriched (Fig. 5b). The Cl is

212   mainly concentrated along the grain boundaries of tuite with some hotspots at the

213   triple junctions (Fig. 5c). The matrix associated with the tuite aggregate is silicate

214   glass characterized by the higher Fe, Mg, Al, and Si contents (compared to tuite)

215   containing several euhedral Si and O rich grains (Fig. 5b-i). The two spots (labelled

216   as 1 and 2 in Fig. 5c) yield a quantitative chemical composition of tuite as

217   determined by the STEM-EDS mapping. Both contain some Cl varying from 0.5 to 7

218   wt% (Table 3).

219   **3.3. High-pressure polymorphs in shock induced melt pocket #2**

220   The shock induced melt pocket #2 (SIMP #2) is located in the interstitial region

221   of pyroxene, which displays common exsolution features with an area of ~ 40 $\times$ 70

222   μm^2 (Figs. 1 and 6). SIMP #2 is mainly composed of silica grains, a relict pyroxene

223   grain, phosphate grains, and the matrix (Fig. 6). There are two types of silica grains,

224   granular in micrometer sizes and tiny euhedral grains (< 1 μm) embedded in the

225   matrix (Fig. 6). The granular silica grains display a strong Raman band at 751 cm^{-1}

226   and two minor ones at 231 and 584 cm^{-1} (Fig. 7e). The phosphate grains in SIMP #2

227   have been transformed into tuite with a strong Raman band at 974 cm^{-1} and several

228   minor bands at 412, 577, 998, and 1095 cm^{-1} (Fig. 7d). The tuite identified in SIMP

229   #2 has a chemical composition (in wt%) of CaO 44.7, P_2O_5 44.2, FeO 3.86, MgO 2.76,

230   SiO_2 2.11, Na_2O 1.56, and minor MnO, Al_2O_3, and K_2O, without detectable F and Cl

231   (Table 2). The relict pyroxene grain in SIMP #2 with exsolution lamellae has Raman

232   bands at 285, 782, and 839 cm^{-1} (Fig. 7c). The chemical composition of the relict

233   pyroxene (in wt%) is SiO_2 48.5, FeO 32.8, MgO 10.4, CaO 5.68, P_2O_5 1.23, and MnO

234   0.84, with minor Al_2O_3, TiO_2, and Na_2O (Table 2).

235   The surrounding pyroxene grains in SIMP #2 are pigeonite and augite as

236   confirmed by Raman (Fig. 7a-b). A FIB foil (FIB #2) on the relict pyroxene was

237 prepared and analyzed using TEM (Fig. 8). FIB #2 is mainly composed of one tuite

238 grain, one relict pyroxene grain (white dashed lines), and the surrounding fine-grained

239 matrix (Fig. 8a-b). The relict pyroxene grain, most likely a pigeonite based on the

240 chemical composition (Table 1), displays well defined augite exsolution lamellae (Fig.

241 8a). The BF-TEM image (Fig. 8c) of the local region outlined in Fig. 8a from the

242 relict pyroxene shows polycrystalline textures. The d-spacings are approximately 2.9

243 and 2.5 Å(Fig. 8d), which are consistent with the (220) and (113) of a spinel phase,

244 respectively. No other diffraction spot or ring was observed (Fig. 8d). The

245 nanocrystals in between the augite exsolution lamellae are less than 50 nm (Fig. 8e-f).

246 The SAED patterns along two different zones shown in Fig. 8e-f are consistent

247 with the crystallography of ahrensite. Two TEM-EDS spots are carried out on the

248 ahrensite and the associated amorphous region (3 and 4 marked in Fig. 8f). The

249 ahrensite grain has a chemical composition (in wt%) of O (38.5), Fe (38.2), Si

250 (15.8), and Mg (7.5) (Table 3). The associated amorphous area has higher Si (34.3),

251 O (54), and Ca (5.0), and lower Fe (8.0) and Mg (1.7) compared with that of the

252 ahrensite grain (Table 3).

4. DISCUSSION

253

4.1. Formation mechanism of tuite in Zagami

254

4.1.1. Decomposition of apatite to tuite in SIMP #1

255

256   The chemical compositions (Tables 1 and 2), textures (Figs. 2 and 4),

257 morphologies (Fig. 5), and Raman analysis (Fig. 3) of the tuite aggregate identified in

258 SIMP #1 indicate that these submicrometer-sized tuite grains were decomposed

259 from a precursor Cl-rich apatite grain. The first reported occurrence of tuite,

260 formed through transformation of apatite, was reported in an ordinary chondrite,

261 Suizhou (Xie et al., 2013). Some chlorapatite grains adjacent to the shock veins in

262 Suizhou were partially decomposed to tuite based on the Raman analysis and lower

263 Cl contents in tuite ($\sim$ 3.2 wt%) than the host apatite ($\sim$ 5.5 wt%) (Xie et

264 al., 2013). The decomposition of apatite to tuite in martian meteorites has

265 only been reported previously in NWA 7755 (Wang et al., 2017). The phosphate

266 aggregate identified in SIMP #1 from Zagami displays diagnostic Raman peaks of

267 tuite (Figs. 2 and 3c) (Xie et al., 2002). The morphology of the tuite aggregate (Fig.

268 2) is more consistent with that of tuite crystals synthesized from chlorapatite (Xie et

269 al., 2013), both displaying subhedral features and compacted with triple junctions. In

addition, the tuite aggregate identified in SIMP #1 from Zagami have some minor

contents of Cl, SiO_2, FeO, MgO,

270   and Al_2O_3, similar to the chemical composition of host apatite (Tables 1 and 2).

271   Furthermore, the adjacent apatite grain to SIMP #1 has also been

272   partially decomposed to tuite (Fig. 2a). These features are nearly identical to the

273   observations of tuite grains, argued for being formed through decomposition of

274   chlorapatite in Suizhou (Xie et al., 2013) and NWA 7755 (Wang et al., 2017).

275   During the decomposition of apatite to tuite [$2Ca_5(PO_4)_3(Cl, F, OH) \rightarrow 3\gamma$-

276    $Ca_3(PO_4)_2 + Ca(Cl, F, OH)_2$], $CaCl_2$, CaF_2, or $Ca(OH)_2$ was expected to be observed

277   associated with tuite (Murayama et al., 1986; Xie et al., 2013). TEM-STEM analyses

278   indicate that the tuite aggregate in SIMP #1 is mainly composed of submicrometer-

279   sized tuite grains with minor Fe-rich hotspots along the tuite grain boundaries, without

280   identification of $CaCl_2$, CaF_2, and $Ca(OH)_2$ (Fig. 5). One possible explanation is that

281   the fractions of $CaCl_2$, CaF_2, and $Ca(OH)_2$ are too small and widely dispersed in the

282   polycrystalline texture of tuite (Murayama et al., 1986). Another possible explanation

283   is that these phases, $e.g.$, $CaCl_2$, are highly soluble in water, and are probably lost

284   during sample preparation (Xie et al., 2013). The Cl content of the tuite aggregate in

285   Zagami is significantly enriched along the grain boundaries of tuite and most enriched

286   at the triple junctions (Fig. 5c). This feature suggests that Cl in the precursor apatite

287   grain was redistributed during decomposition. On the other hand, the ideal molecular

288   formula of tuite, γ-$Ca_3(PO_4)_2$, is incompatible with Cl^-, F^-, and OH^- (Jolliff et al.,

289   2006; McCubbin et al., 2014; Murayama et al., 1986; Xie et al., 2013). TEM-EDS

290   analytical results show that the tuite grains have minor Cl (~ 0.5 wt%), which is much

291   lower than at the triple junctions (~ 7 wt%) (Table 3) and the host apatite (~ 2.3 wt%)

292   (Table 2), probably due to the signal of a nearby/underlying Cl-bearing phase. This

293   observation strongly indicate that the products of apatite decomposition, $e.g.$, $CaCl_2$,

294   could be partially retained in tuite grains because of short duration of asteroid impact

295   and a relatively short post-shock cooling time period (Beck et al., 2005; Ma et al.,

296   2016; Walton et al., 2014). We propose that decomposition of apatite under high-

297   pressure and high-temperature conditions could form a variety of phases on

298   nanometer size scale. The tuite nanophases grew to larger sizes incorporating other

299   products within them simultaneously accompanied with the outwards Cl diffusion

300   because of its incompatible nature in tuite. The other decomposition products of

301   apatite except tuite are mainly concentrated along the grain boundaries of tuite and

302   potentially they were dissolved by water used for sample

303   preparation or were lost with the water vapor during decomposition of the precursor

304   apatite $[Ca(OH)_2 \rightarrow CaO + H_2O]$ if it had some hydroxyl-component (Xie et al.,

305   2016).

306   **4.1.2. Transformation from merrillite to tuite in SIMP #2**

307   The tuite grains identified in SIMP #2 display granular textures with grain sizes

308   ranging from ~ 3 to ~ 10 μm in length (Fig. 6). These tuite grains have minor Na_2O

309   (1.56 wt%), MgO (2.76 wt%), and FeO (3.86 wt%) without detectable Cl and F,

310   nearly identical to the chemical compositions of merrillite (Table 1). Such chemical

311   and morphological features are consistent with previously reported tuite in some

312   martian meteorites (Baziotis et al., 2013; Boonsue and Spray, 2012; Fritz and

313   Greshake, 2009; Malavergne et al., 2001; Miyahara et al., 2016), indicating that they

314   were directly transformed from precursor merrillite grains. The tuite grains identified

315   in SIMP #2 likely did not experienced melting during their formation based on the

316   granular textures, probably attributed to the heterogeneous heat distribution in this

317   melt pocket (Hu and Sharp, 2017).

318   **4.2. Formation mechanism of ahrensite: Decomposition of pigeonite**

319   Raman analysis (Fig. 7) and TEM-SAED patterns (Fig. 8) of the pyroxene clast

320   in SIMP #2 strongly suggest that ahrensite identified here is a high-pressure

321   polymorph of olivine rather than a high-pressure polymorph of pyroxene. The

322   strongest Raman band position on this clast is 839 cm^{-1}, corresponding to a fayalite

323   content of ~ 65 mol % (Feng et al., 2011), which is consistent with the TEM-EDS

324   analysis on the crystalline nanophases from FIB #2 (Table 3). Both the chemical

325   compositions and Raman spectra of the pyroxene clast reveal that it should be an

326   ahrensite grain (Ma et al., 2016).

327   Ahrensite and ringwoodite are the Fe- and Mg-endmember of γ-$(Mg, Fe)_2SiO_4$,

328   respectively (Ma et al., 2016; Tomioka and Miyahara, 2017). The commonly

329   identified olivine high-pressure polymorph is ringwoodite in martian meteorites Dar

330   al Gani (DaG) 670 (Greshake et al., 2013), Elephant Moraine (EET) A79001

331   (Miyahara et al., 2016; Walton, 2013), NWA 4468 (Boonsue and Spray, 2012), NWA

332   7755 (Wang et al., 2017), Grove Mountains (GRV) 020090 (Lin et al., 2011),

333   Tissint (Ma et al., 2016), and Chassigny (Fritz and Greshake, 2009). To date,

334   Tissint and NWA 8159 were reported to contain ahrensite (Ma et al., 2016; Sharp et

335   al., 2019). All of these martian meteorites contain abundant igneous olivine

    macrocrystals (Boonsue

336   and Spray, 2012; Fritz and Greshake, 2009; Greshake et al., 2013; Lin et al., 2011; Ma

337   et al., 2016; Miyahara et al., 2016; Sharp et al., 2019; Wang et al., 2017). In contrast,

338   olivine is rare in the basaltic shergottites including Zagami, except where it occurs in

339   trace amounts through decomposition of late-crystallized Fe-rich pyroxene grains into

340   Fe-rich olivine, hedenbergite and silica (Wadhwa et al., 1993). There are no olivine

341   grains identified across the Zagami section used in this study (Fig. 1). The pyroxene

342   clast with Raman diagnostic bands of ahrensite in SIMP #2 is likely not related to the

343   transformation of olivine as supported by the identical morphologic texture to the

344   adjacent pigeonite with well defined augite exsolution lamellae (Fig. 6). This

345   inference is further supported by its identical chemical composition to pigeonite

346   (Table 2). These characteristics indicate that ahrensite identified in SIMP #2 from

347   Zagami was a decomposition product of pigeonite by solid state transformation under

348   high-pressure and high-temperature conditions.

349   The more detailed TEM-EDS analysis on the major components, ahrensite

350   nanograins and amorphous silicate groundmass in the pyroxene clast reveals that

351   elements of Fe, Mg, and Ca might have been redistributed between the ahrensite

352   nanograins and the groundmass (Table 3). The ahrensite grains have higher Fe

353   contents (Fa ~ 65 mol%) than that of the associated amorphous groundmass and the

354   pyroxene clast (Fe/(Fe + Mg) = 48 mol%) (Tables 2 and 3). One possible explanation

355   is that Fe is more compatible in ahrensite than in pyroxene (Miyahara et al., 2009;

356   Miyahara et al., 2008). During the decomposition of pigeonite, $(Fe,Mg,Ca)SiO_3 \rightarrow$

357   γ- $(Fe,Mg)_2SiO_4 + SiO_2 + CaSiO_3$, most Fe in the pigeonite clast would have been

358   partitioned into ahrensite, leaving the groundmass relatively Fe- and Mg-poorer and

359   Ca-richer than the pyroxene clast (Tables 2 and 3). There are no $CaSiO_3$ perovskite or

360   any high-pressure phases of silica (*e.g.*, stishovite) identified in pyroxene clast (Fig. 8),

361   which is probably because they were not stable to ambient conditions (Martinez et al.,

362   2019; Tomioka and Kimura, 2003).

363   **4.3. P-T-t Constraints**

364   Two high-pressure minerals, tuite and ahrensite (Figs. 2, 3, 6, and 7), are identified

365   in this study from the Zagami basaltic shergottite. The multiple high-pressure minerals,

366   intergrowth of seifertite and stishovite co-occurring in the adjacent silica grain to

367   SIMP #1 indicate that the peak pressure was ~ 22-30 GPa (Bläß, 2013; El Goresy et

368   al., 2008; Langenhorst and Deutsch, 2012; Ma et al., 2018). The apatite grain enclosed

369   by stishovite and seifertite intergrowth (R8 in Fig. 2a) did not transform to tuite (Fig.

370   3d). Another apatite grain, closer to SIMP #1 has partially transformed to tuite (Fig.

371   2a). These features indicate that the shock-induced temperature in the adjacent area to

372   SIMP #1 had a large temperature gradient and was lower than ~ 1000 °C (Murayama

373   et al., 1986). The SIMP #1 was at least partially melted based on the textures and

374   presence of abundant acicular stishovite grains (Fig. 2). The tuite aggregate,

375   recrystallized stishovite grains, and granular stishovite co-existing in SIMP #2 (Fig. 2)

376   requires the shock pressure and temperature of ~ 12-22 GPa and > 1100 °C (El Goresy

377   et al., 2013; Hu and Sharp, 2017; Langenhorst and Deutsch, 2012; Murayama et al.,

378   1986; Sharp et al., 2019; Xie et al., 2016), respectively. These constraints reveal that

379   the P-T conditions of the shock metamorphism experienced by Zagami were

380   heterogeneously distributed in a very limited area. This observation is consistent with

381   other studies of the distribution of high-pressure phases in meteorites and

382   considerations of how shock waves propagate in heterogeneous target

383   materials (Sharp and DeCarli, 2006).

384   There are four types of high-pressure phases: granular tuite and stishovite,

385   euhedral stishovite, and ahrensite coexisting in SIMP #2 (Figs. 6 and 7). Most

386   domains in SIMP #2 have been melted based on the textures except some relict

387   mineral clasts (Fig. 6). The absence of majorite suggests a relatively lower formation

388   temperature (Akaogi et al., 2004). These characteristics indicate that the pressure and

389   temperature of the shock metamorphism in SIMP #2 should be ~12-22 GPa and ~

390   1100-1500 ℃ (Fig. 9) (El Goresy et al., 2013; Hu and Sharp, 2017; Langenhorst and

391   Deutsch, 2012; Ma et al., 2018; Murayama et al., 1986; Sharp et al., 2019; Tschauner

392   et al., 2021; Xie et al., 2016), respectively, which is consistent with the estimates for

393   the surrounding of hotspots where liebermannite and stöfflerite formed (Ma et al.,

394   2018; Tschauner et al., 2021), in accordance with the fact that the kinetic

395   transformation boundaries are both time- and temperature-dependent (Ma et al.,

396   2016).

397   Previous studies on Zagami shergottite have identified six high-pressure minerals,

398   stishovite (Langenhorst and Poirier, 2000b), seifertite (El Goresy et al., 2008),

399   liebermannite (Ma et al., 2018), zagamiite-donwilhelmsite (Beck et al., 2004; Fritz et

400   al., 2020; Tschauner and Ma, 2017), and akimotoite (Langenhorst and Poirier, 2000b).

401   A peak-shock pressure in Zagami was estimated to be ~ 30 GPa based on inferred

14

402 shock barometers (Langenhorst and Poirier, 2000a; Langenhorst et al., 1991). The

403 shock pressure and temperature estimated from the high-pressure mineral assemblage

404 are about 20-22 GPa and 1900 ~ 2200 °C (Beck et al., 2004; El Goresy et al., 2000a;

405 El Goresy et al., 2008; El Goresy et al., 2013), respectively. Such P-T conditions are

406 slightly higher than the estimates in this work. The reason is the fact that the P-T

407 conditions estimated are for local hotspots rather than the peak shock conditions (Fritz

408 et al., 2017; Ma et al., 2018; Tschauner et al., 2021). This lower shock temperature

409 might offset the kinetic transformation boundaries from the bulk rock shock peak

410 pressure (20 to < 30 GPa) and the reactions which occur at lower static equilibrium

411 pressures were observed. Another possibility is that the parent rock derived from

412 regions outside the isobaric core, where shock wave has lost its broad pressure plateau,

413 and mineral assemblages in shock melt pockets form at a lower shock pressure (Fritz

414 et al., 2017). The cooling time of the melt pockets is estimated to be ~2 ms by thermal

415 conduction equation (Fritz and Greshake, 2009) and ~3 ms by HEAT program (Shaw

416 and Walton, 2013). The smaller melt pockets could have quenched more rapidly and

417 easily compared with the larger ones (Hu and Sharp, 2017; Sharp et al., 2019). In

418 addition, the nanometer sizes of ahrensite might further support a fast postshock

419 cooling rate.

5. Implications

421   Most high-pressure minerals found in shocked meteorites were formed either by

422 crystallization from melts or via solid state transformation from their precursor phases.

423 The discovery of tuite aggregate in SIMP #1 and ahrensite in SIMP #2 could shed

424 light on the phase decomposition under high P-T conditions. During the

425 shock-induced decomposition of apatite, the hydroxyl and halogen bearing products

426 would be mobilized and then concentrated along the grain boundaries of tuite grains.

427 Although this study did not definitely confirm the dissociation product of apatite,

428 $CaCl_2$, the Cl-rich phases along the grain boundary of tuite is the most plausible

429 candidate to $CaCl_2$. A more detailed experimental setup is required to make a further

430 confirmation, for instance, a water-free sample preparation protocol to avoid dissolve

431 of $CaCl_2$. Nanocrystalline ahrensite that identified in the pyroxene clast from Zagami is

432 likely the product of decomposition of pigeonite under high P-T conditions through a

433 solid state transformation mechanism. This dissociation of pigeonite to

434 ahrensite/ringwoodite plus other phases may be widespread in other heavily shocked

435 meteorites but potentially been overlooked in previous studies.

436

ACKNOWLEDGEMENTS

447

REFERENCES

449 Akaogi, M., Yano, M., Tejima, Y., Iijima, M., and Kojitani, H. (2004) High-pressure
450   transitions of diopside and wollastonite: phase equilibria and thermochemistry of
451      $CaMgSi_2O_6$, $CaSiO_3$ and $CaSi_2O_5$–$CaTiSiO_5$ system. Physics of the Earth and
452   Planetary Interiors, 143, 145-156.
453 Baziotis, I.P., Liu, Y., DeCarli, P.S., Melosh, H.J., McSween, H.Y., Bodnar, R.J., and
454   Taylor, L.A. (2013) The Tissint Martian meteorite as evidence for the largest
455   impact excavation. Nature Communications, 4, 1404.
456 Beck, P., Gillet, P., El Goresy, A., and Mostefaoui, S. (2005) Timescales of shock
457   processes in chondritic and martian meteorites. Nature, 435(7045), 1071-1074.
458 Beck, P., Gillet, P., Gautron, L., Daniel, I., and El Goresy, A. (2004) A new natural
459   high-pressure (Na,Ca)-hexaluminosilicate $[(Ca_xNa_{1-x})Al_{3+x}Si_{3-x}O_{11}]$ in shocked
460   Martian meteorites. Earth and Planetary Science Letters, 219(1-2), 1-12.
461 Binns, R., Davis, R., and Reed, S. (1969) Ringwoodite, natural (Mg, Fe)$_2$SiO$_4$ spinel
462   in the Tenham meteorite. Nature, 221(5184), 943-944.
463 Bläß, U.W. (2013) Shock-induced formation mechanism of seifertite in shergottites.
464   Physics and Chemistry of Minerals, 40(5), 425-437.
465 Boonsue, S., and Spray, J. (2012) Shock-Induced Phase Transformations in Melt
466   Pockets within Martian Meteorite NWA 4468. Spectroscopy Letters, 45,
467   127-134.
468 Chen, M., El Goresy, A., and Gillet, P. (2004) Ringwoodite lamellae in olivine: Clues
469   to olivine-ringwoodite phase transition mechanisms in shocked meteorites and
470   subducting slabs. Proceedings of the National Academy of Science, 101(42),
471   15033-7.
472 Chen, M., Sharp, T.G., El Goresy, A., Wopenka, B., and Xie, X. (1996) The
473   majorite-pyrope + magnesiowüstite assemblage: Constraints on the history of
474   shock veins in chondrites. Science, 271(5255), 1570-1573.

475   Chen, M., Shu, J., Mao, H.-k., Xie, X., and Hemley, R.J. (2003) Natural occurrence
476   and synthesis of two new postspinel polymorphs of chromite. Proceedings of the
477   National Academy of Sciences, 100(25), 14651-14654.
478   El Goresy, A., Chen, M., Gillet, P., and Dubrovinsky, L.S. (2000a) Shock-induced
479   high-pressure phase transition of labradorite to hollandite "(Na-47-Ca-51-K-2)"
480   in Zagami and the assemblage hollandite "(Na-80-Ca-12-K-8)" plus jadeite in L
481   chondrites: Constraints to peak shock pressures. Meteoritics & Planetary Science,
482   35, A51.
483   El Goresy, A., Dera, P., Sharp, T.G., Prewitt, C.T., Chen, M., Dubrovinsky, L.,
484   Wopenka, B., Boctor, N.Z., and Hemley, R.J. (2008) Seifertite, a dense
485   orthorhombic polymorph of silica from the Martian meteorites Shergotty and
486   Zagami. European Journal of Mineralogy, 20(4), 523-528.
487   El Goresy, A., Dubrovinsky, L., Sharp, T.G., and Chen, M. (2004) Stishovite and
488   post-stishovite polymorphs of silica in the shergotty meteorite: their nature,
489   petrographic settings versus theoretical predictions and relevance to Earth's
490   mantle. Journal of Physics and Chemistry of Solids, 65(8-9), 1597-1608.
491   El Goresy, A., Dubrovinsky, L., Sharp, T.G., Saxena, S.K., and Chen, M. (2000b) A
492   Monoclinic Post-Stishovite Polymorph of Silica in the Shergotty Meteorite.
493   Science, 288, 1632-1635.
494   El Goresy, A., Gillet, P., Miyahara, M., Ohtani, E., Ozawa, S., Beck, P., and
495   Montagnac, G. (2013) Shock-induced deformation of Shergottites:
496   Shock-pressures and perturbations of magmatic ages on Mars. Geochimica et
497   Cosmochimica Acta, 101, 233-262.
498   Feng, L., Lin, Y., Hu, S., Xu, L., and Miao, B. (2011) Estimating compositions of
499   natural ringwoodite in the heavily shocked Grove Mountains 052049 meteorite
500   from Raman spectra. American Mineralogist, 96, 1480-1489.
501   Fritz, J., and Greshake, A. (2009) High-pressure phases in an ultramafic rock from
502   Mars. Earth and Planetary Science Letters, 288(3-4), 619-623.
503   Fritz, J., Greshake, A., and Fernandes, V.A. (2017) Revising the shock classification
504   of meteorites. Meteoritics & Planetary Science, 52(6), 1216-1232.
505   Fritz, J., Greshake, A., Klementova, M., Wirth, R., Palatinus, L., Trønnes, R.G.,
506   Fernandes, V.A., Böttger, U., and Ferrière, L. (2020) Donwilhelmsite,
507   [$CaAl_4Si_2O_{11}$], a new lunar high-pressure Ca-Al-silicate with relevance for
508   subducted terrestrial sediments. American Mineralogist, 105(11), 1704-1711.
509   Gasparik, T. (1990) Phase relations in the transition zone. Journal of Geophysical
510   Research: Solid Earth, 95(B10), 15751-15769.
511   Gillet, P., Chen, M., Dubrovinsky, L., and El Goresy, A. (2000) Natural
512         $NaAlSi_3O_8$-hollandite in the shocked Sixiangkou meteorite. Science, 287(5458),
513   1633-1636.
514   Glass, B.P., Liu, S., and Leavens, P.B. (2002) Reidite: An impact-produced
515   high-pressure polymorph of zircon found in marine sediments. American
516   Mineralogist, 87(4), 562-565.
517   Greshake, A., Fritz, J., Böttger, U., and Goran, D. (2013) Shear-induced ringwoodite
518   formation in the Martian shergottite Dar al Gani 670. Earth and Planetary
519   Science Letters, 375, 383-394.
520   Hu, J., and Sharp, T.G. (2016) High-pressure phases in shock-induced melt of the
521   unique highly shocked LL6 chondrite Northwest Africa 757. Meteoritics &
522   Planetary Science, 51(7), 1353-1369.

523 Hu, J.P., and Sharp, T.G. (2017) Back-transformation of high-pressure minerals in
524   shocked chondrites: Low-pressure mineral evidence for strong shock.
525   Geochimica et Cosmochimica Acta, 215, 277-294.
526 Hu, S., Li, Y., Gu, L., Tang, X., Zhang, T., Yamaguchi, A., Lin, Y., and Changela, H.
527   (2020) Discovery of coesite from the martian shergottite Northwest Africa 8657.
528   Geochimica et Cosmochimica Acta, 286, 404-407.
529 Jolliff, B.L., Hughes, J.M., Freeman, J.J., and Zeigler, R.A. (2006) Crystal chemistry
530   of lunar merrillite and comparison to other meteoritic and planetary suites of
531   whitlockite and merrillite. American Mineralogist, 91(10), 1583-1595.
532 Kayama, M., Tomioka, N., Ohtani, E., Seto, Y., Nagaoka, H., Gotze, J., Miyake, A.,
533   Ozawa, S., Sekine, T., Miyahara, M., Tomeoka, K., Matsumoto, M., Shoda, N.,
534   Hirao, N., and Kobayashi, T. (2018) Discovery of moganite in a lunar meteorite
535   as a trace of H_2O ice in the Moon's regolith. Science advances, 4(5), eaar4378.
536 Langenhorst, F., and Deutsch, A. (2012) Shock Metamorphism of Minerals. Elements,
537   8(1), 31-36.
538 Langenhorst, F., and Poirier, J.-P. (2000a) 'Eclogitic' minerals in a shocked basaltic
539   meteorite. Earth and Planetary Science Letters, 176(3-4), 259-265.
540 Langenhorst, F., and Poirier, J.P. (2000b) Anatomy of black veins in Zagami: clues to
541   the formation of high-pressure phases. Earth and Planetary Science Letters,
542   184(1), 37-55.
543 Langenhorst, F., Stöffler, D., and Klein, D. (1991) Shock metamorphism of the
544   Zagami achondrite. Lunar and Planetary Science Conference, 22.
545 Lin, Y., Feng, L., and Hu, S. (2011) High pressure mineral assemblages in the
546   lherzolitic shergottite Grove Mountains (GRV) 020090. Japan Geoscience Union
547   meeting, #PPS05-03, Tokyo.
548 Litasov, K.D., and Podgornykh, N.M. (2017) Raman spectroscopy of various
549   phosphate minerals and occurrence of tuite in the Elga IIE iron meteorite. Journal
550   of Raman Spectroscopy, 48(11), 1518-1527.
551 Liu, L.-G. (1978) High-pressure phase transformations of albite, jadeite and nepheline.
552   Earth and Planetary Science Letters, 37, 438-444.
553 Ma, C. (2018) A closer look at shocked meteorites: Discovery of new high-pressure
554   minerals. American Mineralogist, 103(10), 1521-1522.
555 Ma, C., Tschauner, O., Beckett, J.R., Liu, Y., Greenberg, E., and Prakapenka, V.B.
556   (2019) Chenmingite, $FeCr_2O_4$ in the $CaFe_2O_4$-type structure, a shock-induced,
557   high-pressure mineral in the Tissint martian meteorite. American Mineralogist:
558   Journal of Earth and Planetary Materials, 104(10), 1521-1525.
559 Ma, C., Tschauner, O., Beckett, J.R., Liu, Y., Rossman, G.R., Sinogeikin, S.V., Smith,
560   J.S., and Taylor, L.A. (2016) Ahrensite, γ-Fe_2SiO_4, a new shock-metamorphic
561   mineral from the Tissint meteorite: Implications for the Tissint shock event on
562   Mars. Geochimica et Cosmochimica Acta, 184, 240-256.
563 Ma, C., Tschauner, O., Beckett, J.R., Liu, Y., Rossman, G.R., Zhuravlev, K.,
564   Prakapenka, V., Dera, P., and Taylor, L.A. (2015) Tissintite, (Ca, Na, $\square$)$AlSi_2O_6$,
565   a highly-defective, shock-induced, high-pressure clinopyroxene in the Tissint
566   martian meteorite. Earth and Planetary Science Letters, 422, 194-205.
567 Ma, C., Tschauner, O., Beckett, J.R., Rossman, G.R., Prescher, C., Prakapenka, V.B.,
568   Bechtel, H.A., and Macdowell, A. (2018) Liebermannite, $KAlSi_3O_8$, a new
569   shock-metamorphic, high-pressure mineral from the Zagami Martian meteorite.
570   Meteoritics & Planetary Science, 53(1), 50-61.

571 Malavergne, V., Guyot, F., Benzerara, K., and Martinez, I. (2001) Description of new
572   shock-induced phases in the Shergotty, Zagami, Nakhla and Chassigny
573   meteorites. Meteoritics & Planetary Science, 36(10), 1297-1305.

574 Martinez, M., Brearley, A.J., Trigo‑Rodríguez, J.M., and Llorca, J. (2019) New
575   observations on high-pressure phases in a shock melt vein in the Villalbeto de la
576   Peña meteorite: Insights into the shock behavior of diopside. Meteoritics &
577   Planetary Science, 54(11), 2845-2863.

578 McCoy, T.J., Taylor, G.J., and Keil, K. (1992) Zagami: Product of a two-stage
579   magmatic history. Geochimica et Cosmochimica Acta, 56(9), 3571-3582.

580 McCubbin, F.M., Shearer, C.K., Burger, P.V., Hauri, E.H., Wang, J., Elardo, S.M., and
581   Papike, J.J. (2014) Volatile abundances of coexisting merrillite and apatite in the
582   martian meteorite Shergotty: Implications for merrillite in hydrous magmas.
583   American Mineralogist, 99(7), 1347-1354.

584 Miyahara, M., El Goresy, A., Ohtani, E., Kimura, M., Ozawa, S., Nagase, T., and
585   Nishijima, M. (2009) Fractional crystallization of olivine melt inclusion in
586   shock-induced chondritic melt vein. Physics of the Earth and Planetary Interiors,
587   177, 116-121.

588 Miyahara, M., El Goresy, A., Ohtani, E., Nagase, T., Nishijima, M., Vashaei, Z.,
589   Ferroir, T., Gillet, P., Dubrovinsky, L., and Simionovici, A. (2008) Evidence for
590   fractional crystallization of wadsleyite and ringwoodite from olivine melts in
591   chondrules entrained in shock-melt veins. Proceedings of the National Academy
592   of Science, 105, 8542-8547.

593 Miyahara, M., Kaneko, S., Ohtani, E., Sakai, T., Nagase, T., Kayama, M., Nishido, H.,
594   and Hirao, N. (2013) Discovery of seifertite in a shocked lunar meteorite. Nature
595   Communications, 4, 1737.

596 Miyahara, M., Ohtani, E., El Goresy, A., Ozawa, S., and Gillet, P. (2016) Phase
597   transition processes of olivine in the shocked Martian meteorite Tissint: Clues to
598   origin of ringwoodite-, bridgmanite- and magnesiowüstite-bearing assemblages.
599   Physics of the Earth and Planetary Interiors, 259, 18-28.

600 Miyahara, M., Ohtani, E., Yamaguchi, A., Ozawa, S., Sakai, T., and Hirao, N. (2014)
601   Discovery of coesite and stishovite in eucrite. Proceedings of the National
602   Academy of Sciences, 111(30), 10939-10942.

603 Murayama, J.K., Nakai, S., Kato, M., and Kumazawa, M. (1986) A dense polymorph
604   of $Ca_3(PO_4)_2$: a high pressure phase of apatite decomposition and its geochemical
605   significance. Physics of the Earth and Planetary Interiors, 44(4), 293-303.

606 Ohtani, E., Ozawa, S., Miyahara, M., Ito, Y., Mikouchi, T., Kimura, M., Arai, T., Sato,
607   K., and Hiraga, K. (2011) Coesite and stishovite in a shocked lunar meteorite,
608   Asuka-881757, and impact events in lunar surface. Proceedings of the National
609   Academy of Science, 108, 463-466.

610 Pang, R.-L., Harries, D., Pollok, K., Zhang, A.-C., and Langenhorst, F. (2018) Vestaite,
611      $(Ti^{4+}Fe^{2+})Ti_3^{4+}O_9$, a new mineral in the shocked eucrite Northwest Africa 8003.
612   American Mineralogist, 103, 1502-1511.

613 Pang, R.-L., Zhang, A.-C., Wang, S.-Z., Wang, R.-C., and Yurimoto, H. (2016)
614   High-pressure minerals in eucrite suggest a small source crater on Vesta.
615   Scientific Reports, 6, 26063.

616 Petrova, E.V., and Grokhovsky, V.I. (2019) High pressure impacts on meteorites. Pure
617   and Applied Chemistry, 91(11), 1857-1867.

618 Putnis, A., Price, G. D., 1979. High-pressure $(Mg, Fe)_2SiO_4$ phases in the Tenham
619   chondritic meteorite. Nature. 280(5719), 217-218.

620 Sharp, T.G., and DeCarli, P.S. (2006) Shock effects in meteorites. Meteorites and the
621   early solar system II, 943, 653-677.
622 Sharp, T.G., El Goresy, A., Wopenka, B., and Chen, M. (1999) A Post-Stishovite SiO2
623   Polymorph in the Meteorite Shergotty: Implications for Impact Events. Science,
624   284, 1511.
625 Sharp, T.G., Lingemann, C.M., Dupas, C., and Stöffler, D. (1997) Natural occurrence
626   of MgSiO3-ilmenite and evidence for MgSiO3-perovskite in a shocked L
627   chondrite. Science, 277(5324), 352-355.
628 Sharp, T.G., Walton, E.L., Hu, J.P., and Agee, C. (2019) Shock conditions recorded in
629   NWA 8159 martian augite basalt with implications for the impact cratering
630   history on Mars. Geochimica Et Cosmochimica Acta, 246, 197-212.
631 Shaw, C.S.J., and Walton, E. (2013) Thermal modeling of shock melts in Martian
632   meteorites: Implications for preserving Martian atmospheric signatures and
633   crystallization of high-pressure minerals from shock melts. Meteoritics &
634   Planetary Science, 48(5), 758-770.
635 Skelton, R., and Walker, A.M. (2017) Ab initio crystal structure and elasticity of tuite,
636   γ-Ca3(PO4)2, with implications for trace element partitioning in the lower
637   mantle. Contributions to Mineralogy and Petrology, 172(10).
638 Stöffler, D., Keil, K., and RD, S.E. (1991) Shock metamorphism of ordinary
639   chondrites. Geochimica et Cosmochimica Acta, 55(12), 3845-3867.
640 Stöffler, D., Ostertag, R., Jammes, C., Pfannschmidt, G., Gupta, P.S., Simon, S.,
641   Papike, J., and Beauchamp, R. (1986) Shock metamorphism and petrography of
642   the Shergotty achondrite. Geochimica et Cosmochimica Acta, 50(6), 889-903.
643 Tomioka, N., and Fujino, K. (1999) Akimotoite,(Mg, Fe)SiO3, a new silicate mineral
644   of the ilmenite group in the Tenham chondrite. American Mineralogist, 84(3),
645   267-271.
646 Tomioka, N., and Kimura, M. (2003) The breakdown of diopside to Ca-rich majorite
647   and glass in a shocked H chondrite. Earth and Planetary Science Letters,
648   208(3-4), 271-278.
649 Tomioka, N., and Miyahara, M. (2017) High-pressure minerals in shocked meteorites.
650   Meteoritics & Planetary Science, 52(9), 2017-2039.
651 Tschauner, O., and Ma, C. (2017) Stöfflerite, IMA 2017-062. CNMNC Newsletter No.
652   39, October 2017. Mineralogical Magazine, 81, 1279-1286.
653 Tschauner, O., Ma, C., Beckett, J.R., Prescher, C., Prakapenka, V.B., and Rossman,
654   G.R. (2014) Discovery of bridgmanite, the most abundant mineral in Earth, in a
655   shocked meteorite. Science, 346(6213), 1100-1102.
656 Tschauner, O., Ma, C., Spray, J.G., Greenberg, E., and Prakapenka, V.B. (2021)
657   Stöfflerite,(Ca, Na)(Si, Al)4O8 in the hollandite structure: A new high-pressure
658   polymorph of anorthite from martian meteorite NWA 856. American
659   Mineralogist: Journal of Earth and Planetary Materials, 106(4), 650-655.
660 Wadhwa, M., McCoy, T.J., Keil, K., and Crozaz, G. (1993) The Chemical and
661   Physical Evolution of Late-Stage Melt in Zagami. Meteoritics, 28, 453-454.
662 Walton, E.L. (2013) Shock metamorphism of Elephant Moraine A79001: Implications
663   for olivine-ringwoodite transformation and the complex thermal history of
664   heavily shocked Martian meteorites. Geochimica et Cosmochimica Acta, 107,
665   299-315.
666 Walton, E.L., Sharp, T.G., Hu, J., and Filiberto, J. (2014) Heterogeneous mineral
667   assemblages in martian meteorite Tissint as a result of a recent small impact
668   event on Mars. Geochimica et Cosmochimica Acta, 140, 334-348.

669 Wang, S.-Z., Zhang, A.-C., Pang, R.-L., Chen, J.-N., Gu, L.-X., and Wang, R.-C.
670   (2017) Petrogenesis and shock metamorphism of the enriched lherzolitic
671   shergottite Northwest Africa 7755. Meteoritics & Planetary Science, 52(11),
672   2437-2457.
673 Xie, X., Gu, X., and Chen, M. (2016) An occurrence of tuite, γ-Ca$_3$(PO$_4$)$_2$, partly
674   transformed from Ca-phosphates in the Suizhou meteorite. Meteoritics &
675   Planetary Science, 51(1), 195-202.
676 Xie, X., Minitti, M.E., Chen, M., Mao, H.-K., Wang, D., Shu, J., and Fei, Y. (2002)
677   Natural high-pressure polymorph of merrillite in the shock veins of the Suizhou
678   meteorite. Geochimica et Cosmochimica Acta, 66(13), 2439-2444.
679 Xie, X., Zhai, S., Chen, M., and Yang, H. (2013) Tuite, γ-Ca$_3$(PO$_4$)$_2$, formed by
680   chlorapatite decomposition in a shock vein of the Suizhou L6 chondrite.
681   Meteoritics & Planetary Science, 48(8), 1515-1523.
682 Xie, Z., and Sharp, T.G. (2007) Host rock solid-state transformation in a
683   shock-induced melt vein of Tenham L6 chondrite. Earth and Planetary Science
684   Letters, 254(3-4), 433-445.
685 Xie, Z., Tomioka, N., and Sharp, T.G. (2002b) Natural occurrence of Fe$_2$SiO$_4$-spinel
686   in the shocked Umbarger L6 chondrite. American Mineralogist, 87(8-9),
687   1257-1260.
688 Xing, W., Lin, Y., Zhang, C., Zhang, M., Hu, S., Hofmann, B.A., Sekine, T., Xiao, L.,
689   and Gu, L. (2020) Discovery of Reidite in the Lunar Meteorite Sayh al Uhaymir
690   169. Geophysical Research Letters, 47(21), e2020GL089583.
691 Zhang, A.-C., Hsu, W.-B., Floss, C., Li, X.-H., Li, Q.-L., Liu, Y., and Taylor, L.A.
692   (2010) Petrogenesis of lunar meteorite Northwest Africa 2977: Constraints from
693   in situ microprobe results. Meteoritics and Planetary Science, 45, 1929-1947.
694 Zhang, J., Li, B., Utsumi, W., and Liebermann, R.C. (1996) In situ X-ray observations
695   of the coesite-stishovite transition: reversed phase boundary and kinetics. Physics
696   and Chemistry of Minerals, 23(1), 1-10.
697
698

699 **Tables**

700

701 Table 1. Representative chemical compositions of pyroxene, maskelynite, merrillite, and apatite from Zagami.

	Pyroxene				Maskelynite				Merrillite				Apatite			
	187	213	227	231	194	195	214	230	198	204	210	225	207	184	196	223
SiO_2	50.8	50.2	50.5	50.9	58.6	57.7	60.1	59.3	0.75	0.43	0.23	0.18	0.90	1.89	0.80	1.00
TiO_2	0.39	0.53	0.54	0.47	0.09	0.12	0.05	0.09	b.d.	0.04	b.d.	b.d.	b.d.	0.05	b.d.	0.08
Al_2O_3	1.24	0.46	0.53	1.04	25.4	24.9	25.7	25.1	0.03	0.03	0.03	b.d.	0.19	0.03	b.d.	0.09
Cr_2O_3	0.53	0.07	0.04	0.42	b.d.	0.04	b.d.	b.d.	0.02	b.d.	b.d.	b.d.	b.d.	b.d.	b.d.	0.04
FeO	19.5	29.8	31.0	20.2	0.70	2.05	0.85	1.48	2.51	3.32	2.80	3.02	0.79	1.90	1.23	1.11
NiO	b.d.	b.d.	b.d.	b.d.	b.d.	b.d.	b.d.	b.d.	b.d.	b.d.	b.d.	b.d.	b.d.	b.d.	0.02	0.00
MnO	0.66	0.84	0.85	0.63	b.d.	0.03	0.04	0.03	0.11	0.14	0.14	0.15	0.08	0.14	0.13	0.12
MgO	11.5	12.8	11.8	12.4	0.08	0.58	0.06	0.30	3.05	2.36	2.44	2.30	0.04	0.45	0.11	0.07
CaO	15.4	5.41	5.11	14.2	8.60	9.12	8.47	8.57	45.9	46.6	46.7	46.9	53.0	53.9	53.0	51.7
Na_2O	0.23	0.10	0.10	0.20	5.55	5.52	5.57	5.74	1.25	1.27	1.49	1.43	0.17	0.06	0.12	0.20
K_2O	b.d.	0.04	0.03	0.03	0.39	0.45	0.48	0.28	b.d.	0.05	0.07	0.05	0.14	b.d.	b.d.	0.13
P_2O_5	0.08	b.d.	0.03	0.07	0.05	0.02	b.d.	b.d.	45.4	45.7	47.3	47.0	43.0	41.0	42.1	42.7
F	b.d.	b.d.	b.d.	b.d.	b.d.	b.d.	b.d.	b.d.	b.d.	b.d.	b.d.	b.d.	1.01	1.81	1.05	0.42
Cl	b.d.	b.d.	b.d.	b.d.	b.d.	b.d.	b.d.	b.d.	0.03	0.02	0.03	0.03	1.53	0.17	1.80	3.37
Total	100.3	100.2	100.6	100.6	99.46	100.6	101.4	100.9	99.07	100.0	101.3	101.1	100.2	100.7	99.7	100.5

702 b.d.: below detection limit.

703

704

22

705 Table 2. EPMA compositions of apatite, merrillite, tuite, ahrensite and pyroxene in

706 shock induced melt pockets #1 and #2 from Zagami.

|	SIMP #1				SIMP #2			
	Apatite	Tuite 1	Tuite 2	Matrix	Tuite-Cl free	Ahrensite	Pigeonite	Augite
SiO_2	2.18	3.02	2.71	56.6	2.11	48.5	49.8	49.8
TiO_2	0.08	0.01	b.d.	0.2	b.d.	0.43	0.47	0.63
Al_2O_3	0.33	0.44	0.27	11.7	0.05	0.4	0.5	0.81
Cr_2O_3	0.02	0.02	0.01	b.d.	b.d.	b.d.	0.06	0.02
FeO	1.52	2.28	1.64	14.3	3.86	32.8	31.3	20.9
NiO	b.d.	0.04	b.d.	b.d.	b.d.	b.d.	b.d.	b.d.
MnO	0.18	0.15	0.12	0.35	0.13	0.84	0.89	0.64
MgO	0.14	0.33	0.15	3.96	2.76	10.4	11.3	10.2
CaO	51.2	49.8	51.1	7.15	44.7	5.68	5.67	16
Na_2O	0.21	0.22	0.17	2.72	1.56	0.06	0.09	0.22
K_2O	b.d.	0.03	b.d.	0.2	0.06	b.d.	b.d.	b.d.
P_2O_5	40.2	39	42.6	1.56	44.2	1.23	0.03	0.43
F	0.69	0.6	0.81	b.d.	b.d.	b.d.	b.d.	b.d.
Cl	2.27	2.15	2.05	0.08	b.d.	b.d.	b.d.	b.d.
Total	98.3	97.4	100.9	98.9	99.4	100.3	100.1	99.6
O=	13	13	13		13	6	6	6
Si	0.2	0.27	0.24		0.18	1.93	1.98	1.95
Ti	0.01	b.d.	b.d.		b.d.	0.01	0.01	0.02
Al	0.04	0.05	0.03		b.d.	0.02	0.02	0.04
Cr	b.d.	b.d.	b.d.		b.d.	b.d.	b.d.	b.d.
Fe	0.11	0.17	0.12		0.27	1.06	1.04	0.68
Ni	b.d.	b.d.	b.d.		b.d.	b.d.	b.d.	b.d.
Mn	0.01	0.01	0.01		0.01	0.03	0.03	0.02
Mg	0.02	0.04	0.02		0.35	0.62	0.67	0.59
Ca	4.96	4.86	4.76		4.02	0.24	0.24	0.67
Na	0.04	0.04	0.03		0.25	b.d.	0.01	0.02
K	b.d.	b.d.	b.d.		0.01	b.d.	b.d.	b.d.
P	3.08	3.01	3.13		3.14	0.04	b.d.	0.01
F	0.2	0.17	0.22		b.d.	b.d.	b.d.	b.d.
Cl	0.35	0.33	0.3		b.d.	b.d.	b.d.	b.d.
Total	8.46	8.46	8.33		8.24	3.99	4	4

707 b.d.: below detection limit.

708

709   Table 3. The chemical compositions (corresponding to Fig. 5c) of tuite and ahrensite

710   measured by TEM-EDS.

	1 (wt%)	2 (wt%)	3 (wt%)	4 (wt%)
Ca	35.1	41.5		5.0
P	22.9	18.9		
Cl	0.5	7.0		
O	41.6	33	38.5	54
Si			15.8	34.3
Mg			7.5	1.7
Fe			38.2	8.0

711

712

713 **Figures**
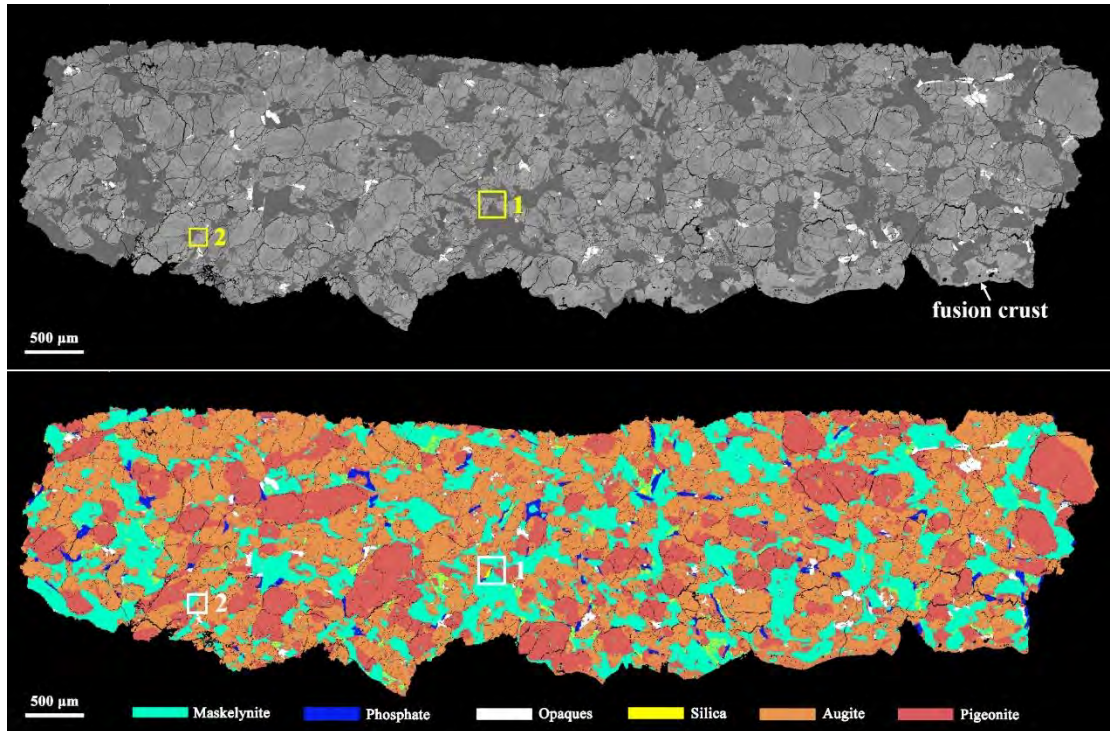
714

715 Figure 1. BSE mosaic image (a) and minerals distribution map (b) of Zagami studied

716 in this work. It consists mainly of pyroxene (augite and pigeonite) and maskelynite,

717 with minor accessory minerals, apatite, merrillite, titanomagnetite, ilmenite, silica,

718 and baddeleyite. Squares (1 and 2) are the locations of shock-induced melt pockets

719 identified in the section.

720

721

722
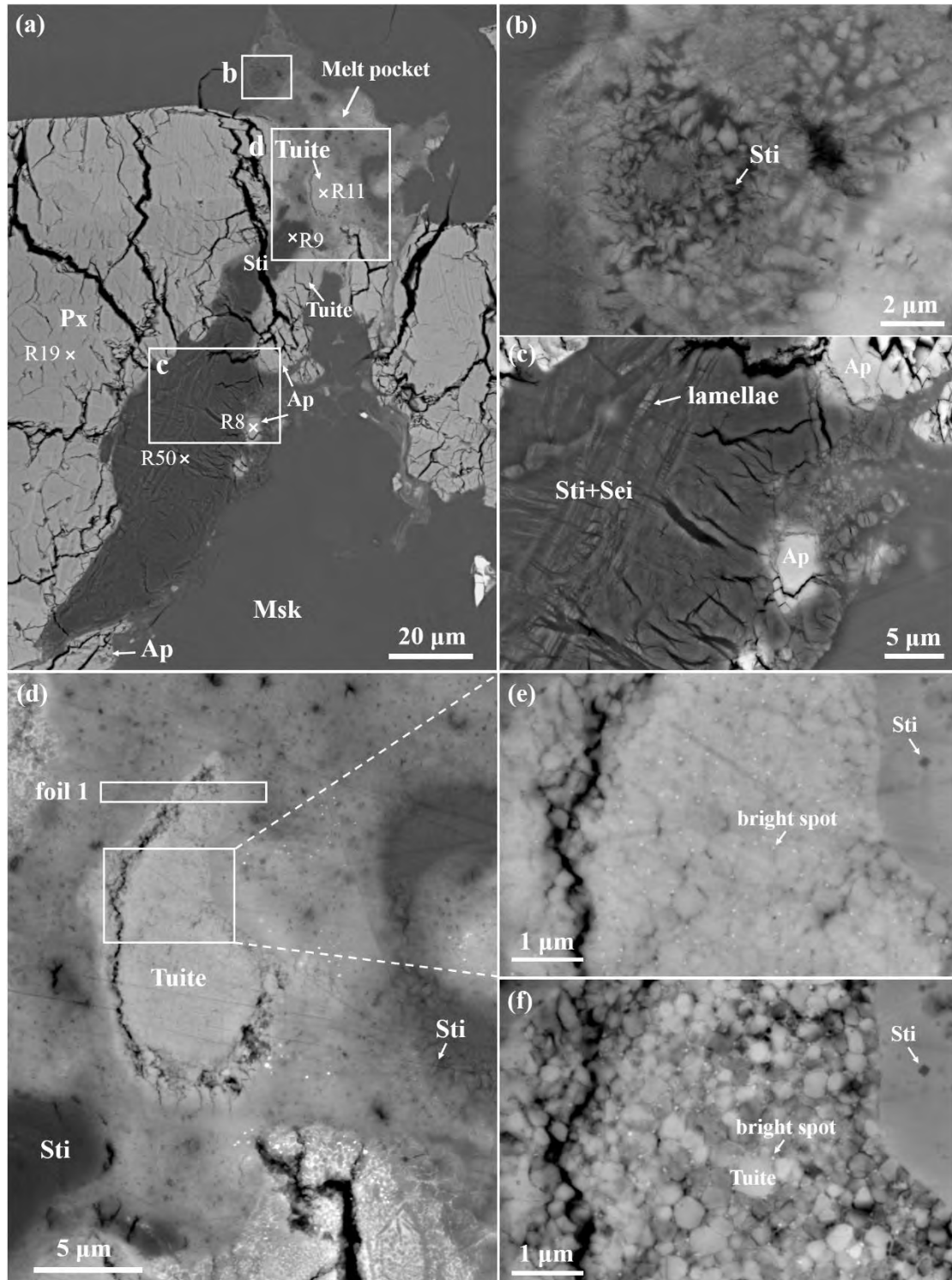
Figure 2. Petrography of shock-induced melt pocket 1 (SIMP #1). (a) SIMP #1 is located at the contact area between pyroxene and maskelynite. A coarse grain of silica at lower left has been transformed into stishovite and seifertite. The white boxes with letters correspond to the areas shown at higher magnification in 2b, 2c and 2d. (b) Acicular stishovite grains in the upper left corner outlined in (a). (c) High

26

728 magnification BSE image of the silica grain showing lamellar texture. (d) Tuite

729 aggregate in SIMP #1. Foil 1 is the location for FIB-TEM analysis. (e) Details of

730 white rectangular region outlined in (d). Tuite, in submicron sizes, is enclosed by

731 silicate glasses in which display nanometer-sized euhedral stishovite grains. Some

732 bright spots are mainly located in the interstitial areas. (f) The morphology of tuite

733 aggregate after bombardment by a laser with energy of 20 mW. Tuite grains are

734 loosely compacted with triple junctions. Px: pyroxene; Sti: stishovite; Ap: apatite;

735 Msk: maskelynite; Sei: seifertite. R+number: Raman analysis location.

736

737
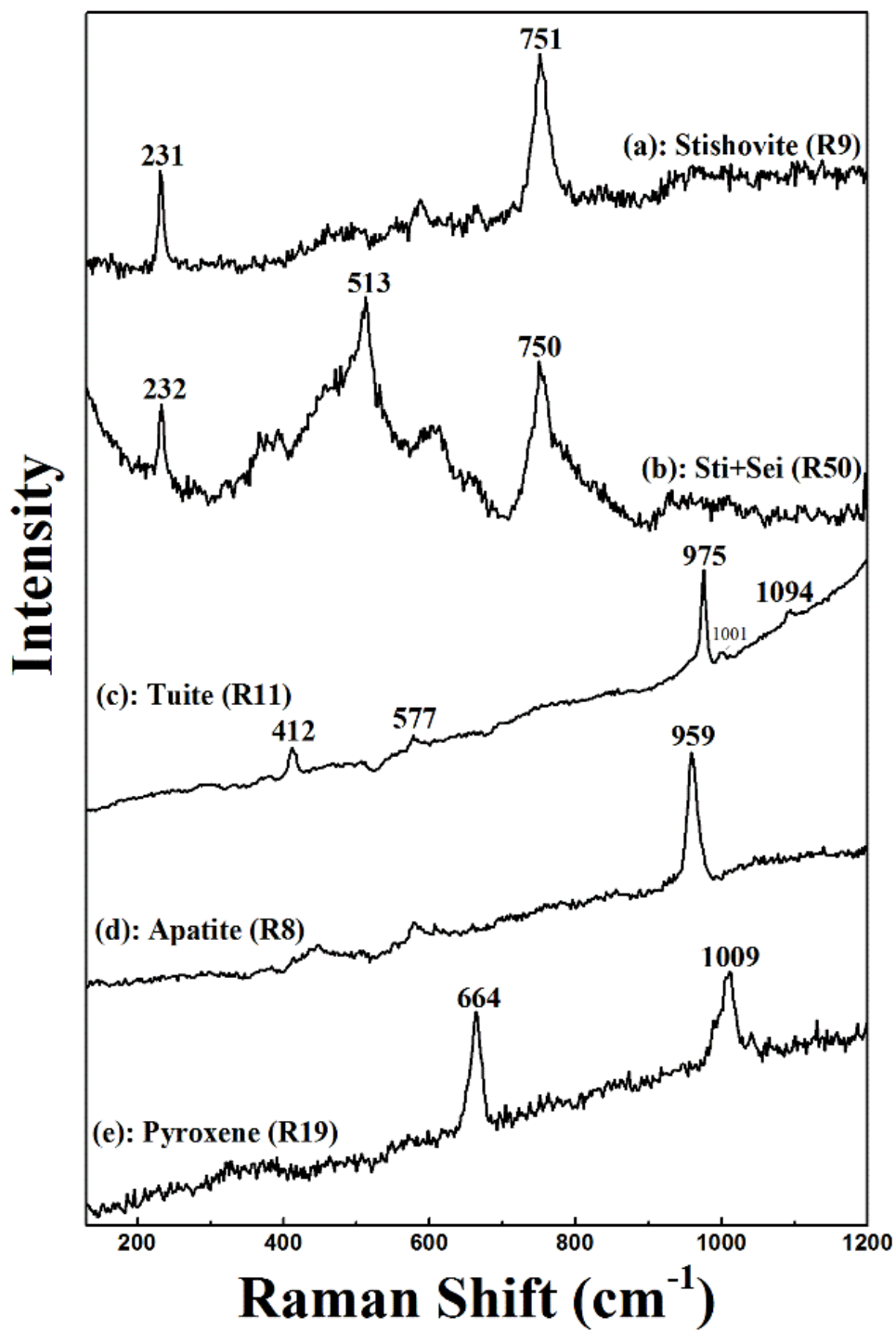
Figure 3. Raman spectra of stishovite (a), intergrowth of stishovite and seifertite (b), tuite (c), apatite (d), and host pyroxene (e) marked in figure 2.
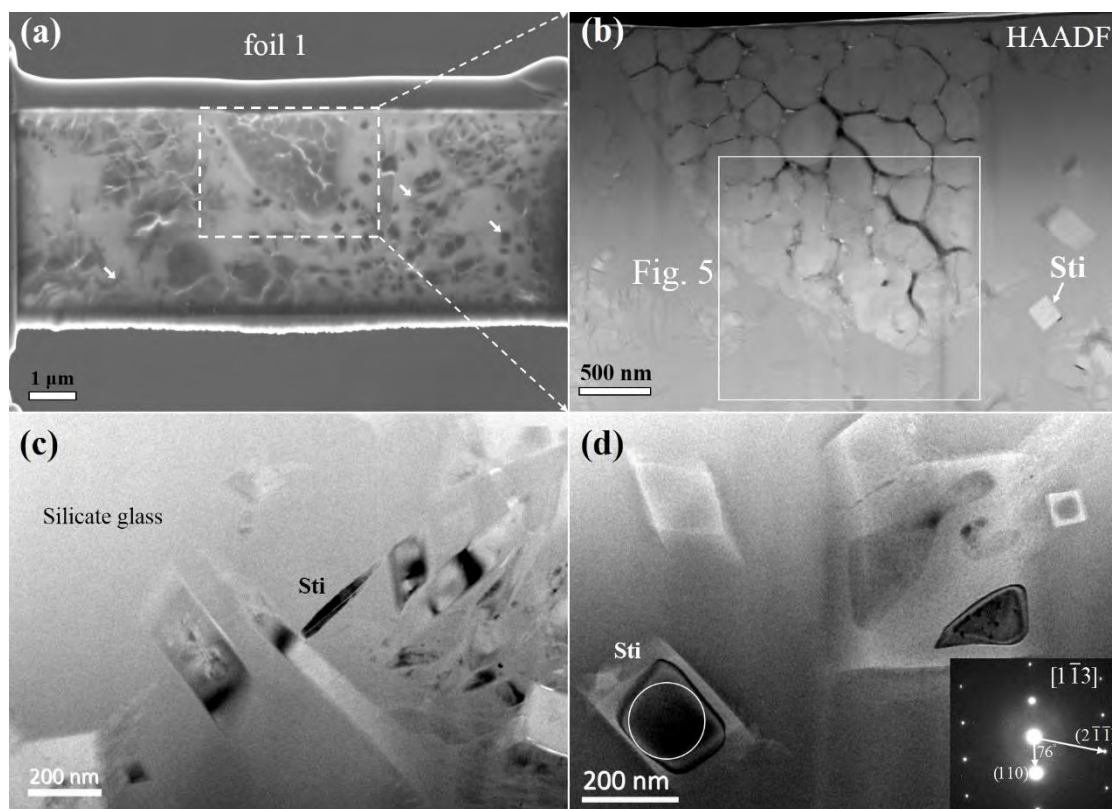
Figure 4. Petrographic textures of FIB foil sample of melt pocket 1 (foil 1). (a) SEM image of cross-section after extraction. The tuite aggregate is enclosed by silicate glasses containing some euhedral silica grains showing darker contrast. (b) HAADF image of tuite aggregate and the associated outer areas. Tuite grains, in nanometer sizes, are compacted showing triple junctions. Some anhedral bright grains are usually found along the grain boundary of tuite. More detailed textures of tuite grains and bright spots are shown in Fig. 5. (c-d) Acicular and euhedral stishovite grains occur in the groundmass of silicate glasses. Inset image in (d) shows the SAED pattern on a stishovite grain from the circled area in (d). The crystal axis calculated to be $[1\bar{1}3]$. Most stishovite grains were easily vitrified under the TEM beam irradiation.
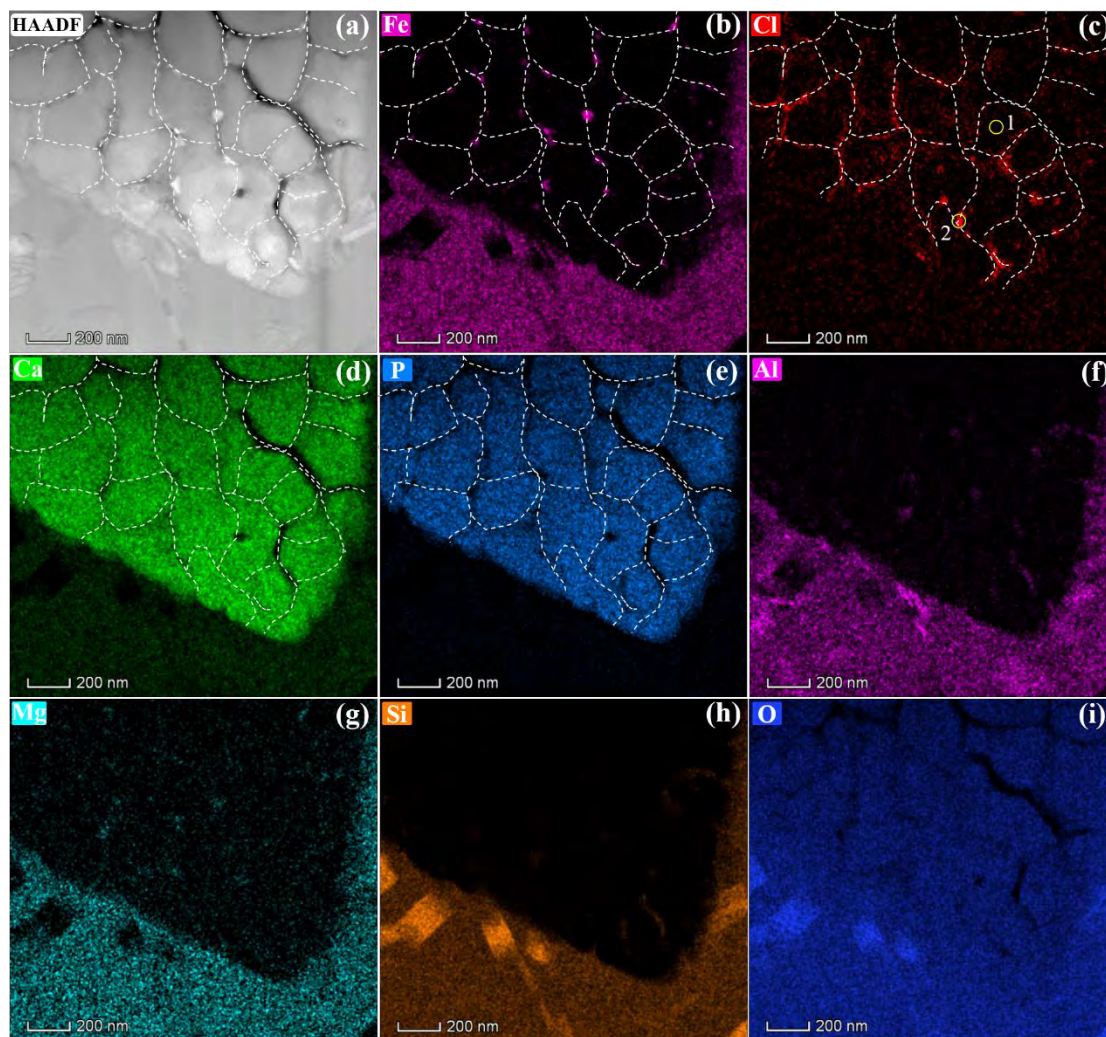
Figure 5. HAADF image (a) and EDS elemental mapping of Fe (b), Cl (c), Ca (d), P (e), Al (f), Mg (g), Si (h), and O (i) of tuite aggregate in foil 1 outlined by the white rectangle in figure 4b. The bright particles in (a) are probably iron oxides (b), which are mainly present along the grain boundary of tuite grains, consistent with the distribution of Cl (c). Stishovite grains in euhedral and acicular shapes are enclosed by the matrix of silicate glasses (g-i). The chemical compositions of Cl hotspot (#2 in (c)) and tuite grain (#1 in (c)) were measured by STEM-EDS and listed in Table 3.
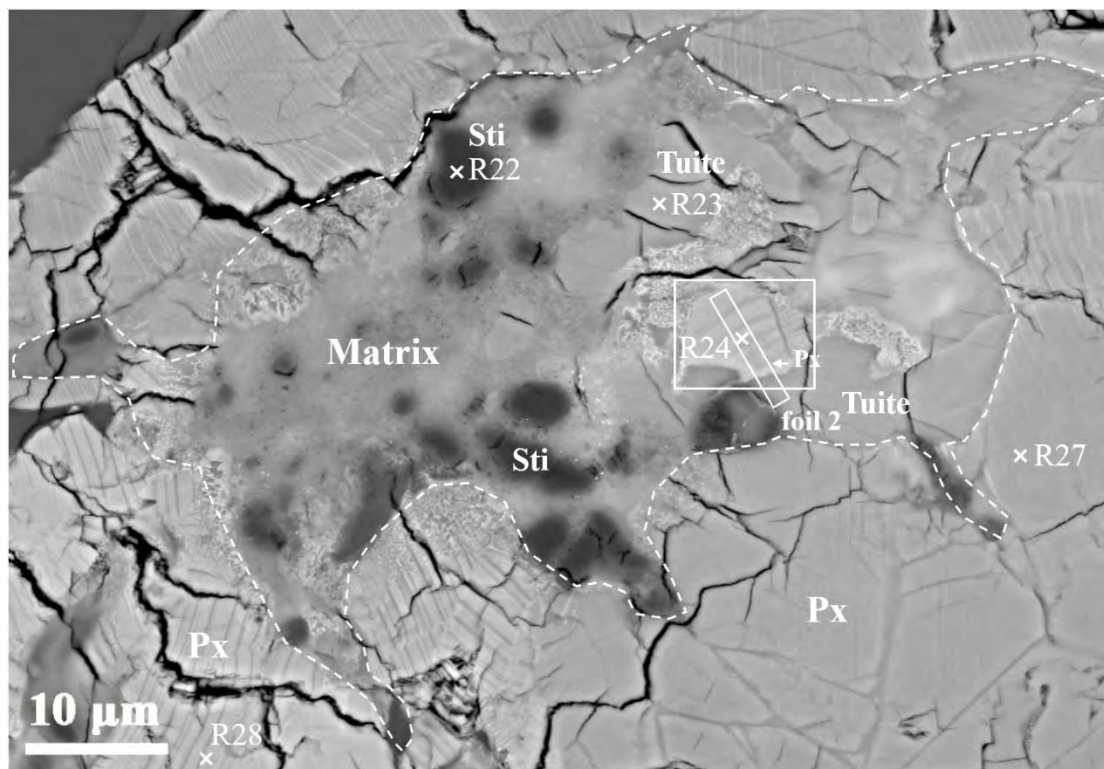
767

768 Figure 6. BSE image of shock induced melt pocket 2 (SIMP #2) outlined by white

769 dashed lines. Pyroxene displays common exsolution lamellae. Micrometer-sized

770 granular aggregates of stishovite grains are occurring on the left side of SIMP #2.

771 Tuite grains are mainly present in areas above to the right of SIMP #2. A pigeonite

772 grain outlined by a white rectangle in melt pocket 2 displays Ca-rich exsolution

773 lamellae, similar to the texture of host pyroxene. However, Raman analysis indicates

774 that this grain has been transformed into ringwoodite/ahrensite. Px: pyroxene; Sti:
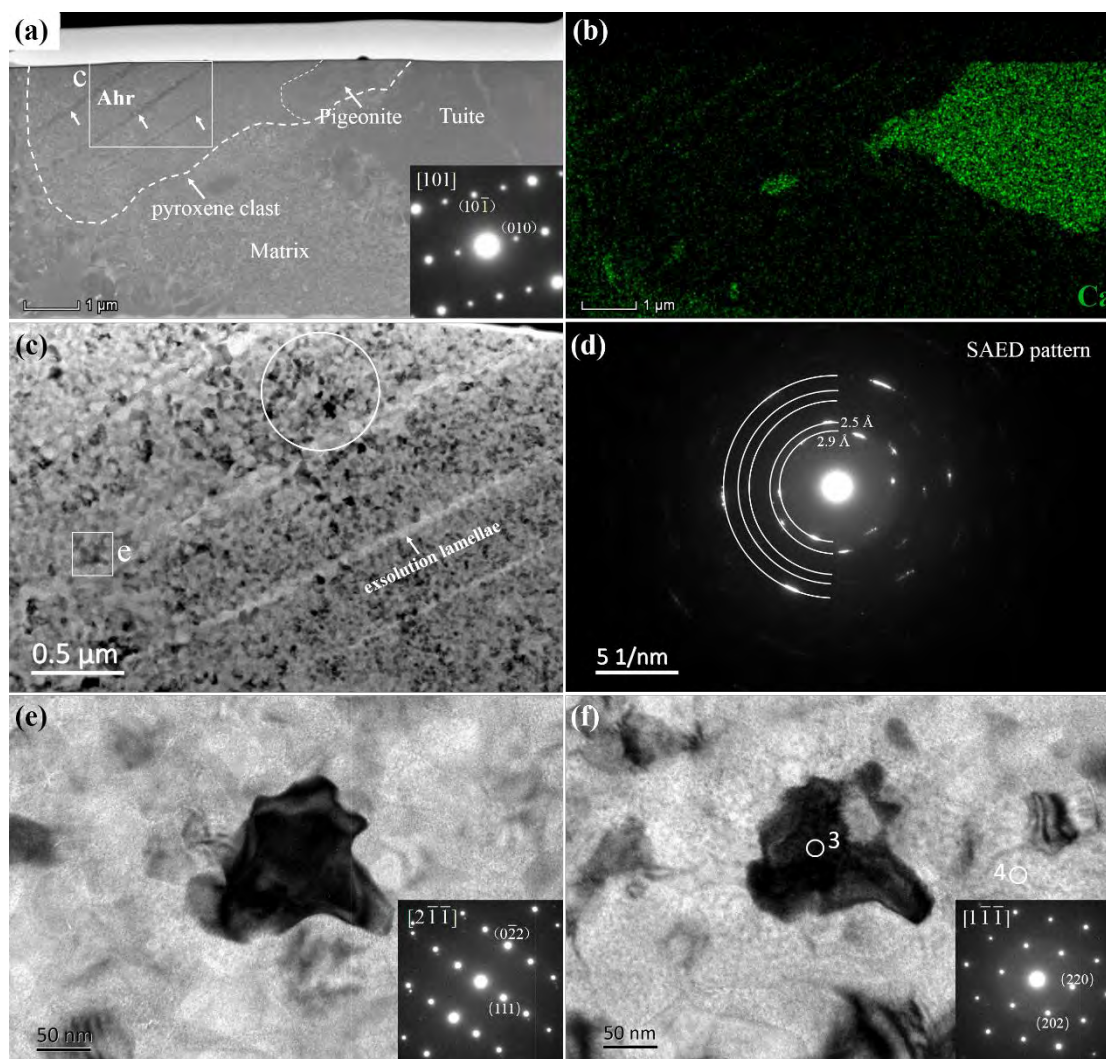
775 stishovite. Ahr: ahrensite.

776

777

778
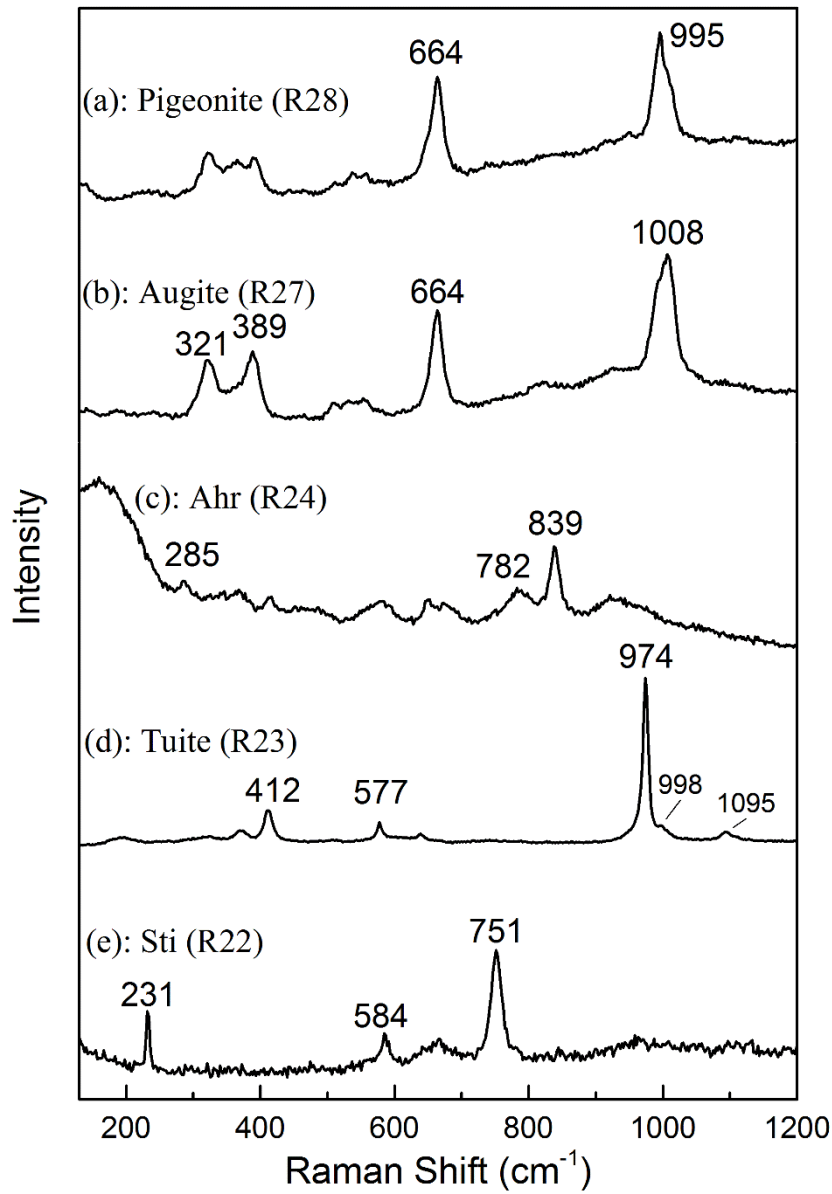
Figure 7. Raman spectra of various phases marked in Fig. 6. (a) pigeonite (R28), (b)

780   augite (R27), (c) ahrensite (R24), (d) tuite (R23), (e) stishovite (R22).

781

782

783

784 Figure 8. (a) HAADF image of foil sample of melt pocket 2 (foil 2), which contains

785 ahrensite, tuite and the associated matrix. (b) Ca element distribution mapping shows

786 that the exsolution lamellae in pigeonite are Ca-rich. (c) TEM image of the

787 fine-grained mineral assemblage. Average grain size is approximately 50 nm. (d) The

788 polycrystalline electron diffraction ring of ahrensite grains. The lattice spaces are 2.9

789 Å and 2.5 Å, respectively. (e) High magnification of one ahrensite grain and its

790 corresponding SAED pattern. (f) Different zone axis of the same grain with (e). The

791 EDS composition of the point 3 is consistent with the ahrensite grain, whereas the

792 point 4 shows SiO_2 rich composition (Table 3). The inset shows the corresponding

793 SAED pattern. Ahr: ahrensite.

794

795
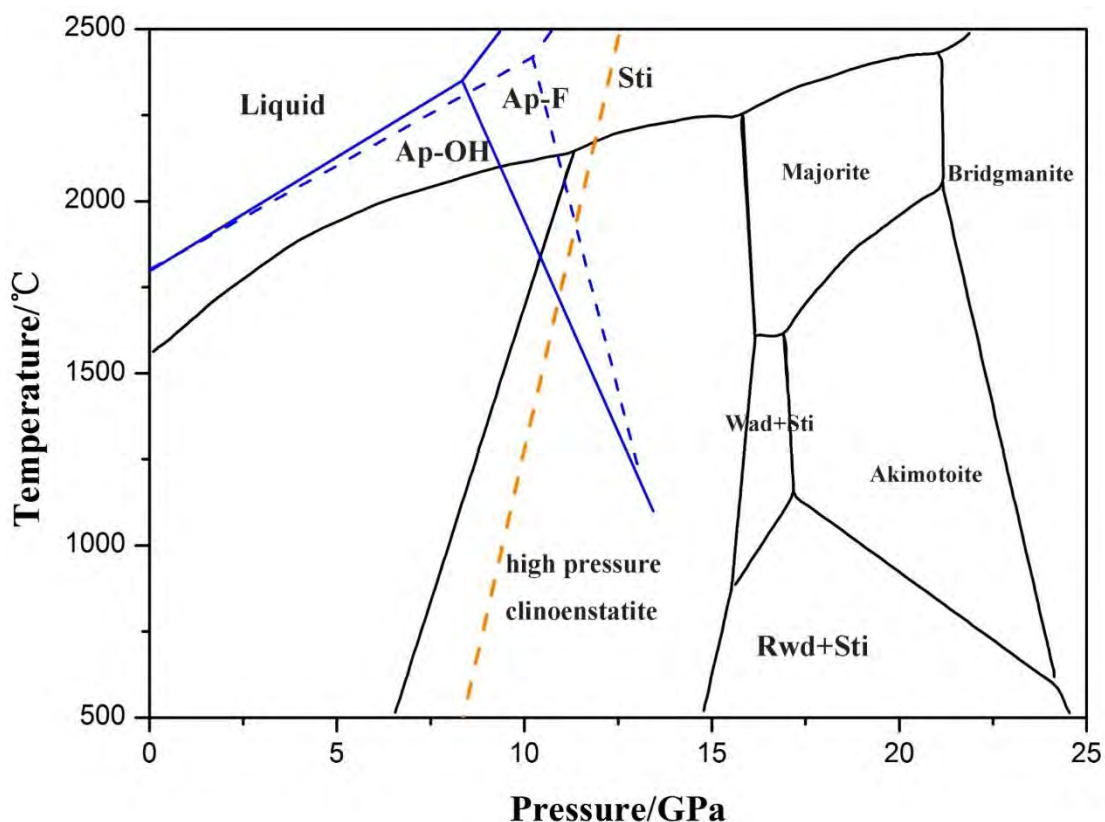
796

797 Figure 9. P-T constraints revealed by the formation of tuite, ahrensite, and stishovite

798 in Zagami meteorite. Black line is the phase diagram of MgSiO₃ (Gasparik, 1990).

799 Blue lines show the stability fields of F- and OH-apatite (Murayama et al., 1986).

800 Orange dashed line is the boundary of coesite and stishovite transformation (Zhang et

801 al., 1996).

802